Pergamon

Geochimica et Cosmochimica Acta, Vol. 66, No. 16, pp. 2841–2853, 2002

0016-7037/02 $22.00 + .00

PII S0016-7037(02)00880-3

Solid-Solution Aqueous-Solution Reactions between Jarosite ($KFe_3(SO_4)_2(OH)_6$) and its Chromate Analog

DIRK BARON*,[1] and CARL D. PALMER[2]

[1]Department of Physics and Geology, California State University, Bakersfield, Bakersfield, CA 93311-1099, USA
[2]Geosciences Research, Idaho National Engineering and Environmental Laboratory, P.O. Box 1625, Idaho Falls, ID 83415-2107, USA

(*Received December* 21, 2000; *accepted in revised form March* 4, 2002)

Abstract—The sulfate mineral jarosite ($KFe_3(SO_4)_2(OH)_6$), its chromate analog ($KFe_3(CrO_4)_2(OH)_6$), and seven precipitates with intermediate compositions ($KFe_3(Cr_XS_{(1-X)}O_4)_2(OH)_6$) were synthesized. The unit cell volume of the precipitates is closely represented by a linear function of composition, suggesting a continuous solid solution. This solid solution dissolves stoichiometrically according to

$$KFe_3(Cr_XS_{(1-X)}O_4)_2(OH)_6 + 6H^+ \leftrightarrow K^+ + 3Fe^{3+} + 2X\ CrO_4^{2-} + (2 - 2X)SO_4^{2-} + 6H_2O$$

and reaches stoichiometric saturation after approximately 40 d. Log K_{SS} values calculated from samples taken after 1090 d are consistently lower than what would be expected for an ideal solid solution, indicating that the excess free energy of mixing, G^E, is negative. G^E calculated from the log K_{SS} values can be closely modeled by the one-parameter Guggenheim expansion

$$G^E = X_{CrJar}\ X_{Jar}\ RT\ a_0$$

where a_0 is -4.9 ± 0.8, X_{CrJar} and X_{Jar} are the mole fractions of $KFe_3(CrO_4)_2(OH)_6$ and $KFe_3(SO_4)_2(OH)_6$ in the solids, R is the gas constant, and T the absolute temperature. Based on the calculated excess free energy, a Lippmann diagram with a modified abscissa was constructed.

1. INTRODUCTION

Chromium is a toxic and carcinogenic metal that is widely used in many industrial processes. It has been released into the environment at many sites, making it a common soil and groundwater contaminant (Calder, 1988; Palmer and Wittbrodt, 1991). Elevated levels of chromium can also result from natural sources like serpentinites in the California Coast Ranges (Rytuba and Kleinkopf, 1995). Because of the potential health hazards associated with chromium, there is interest in understanding the processes that control its mobility in the environment to assess the risks associated with Cr releases and to design effective clean-up measures for chromium-contaminated sites. A key process affecting chromium mobility in the subsurface is the precipitation of chromium-containing solid phases. These solids can form as chromate-laden solutions interact with soils, changing their chemical environment and causing the dissolution of native soil minerals and the subsequent precipitation of new phases. These chromium-containing solids can form as pure phases or as solid solutions with common soil minerals. Examples of such solid solutions include $Fe_XCr_{(1-X)}(OH)_3$ which is thought to control the concentrations of Cr(III) in soils under alkaline to slightly acidic conditions (Rai et al., 1987; Sass and Rai, 1987; Amonette and Rai, 1990), and $Ba(Cr_XS_{(1-X)})O_4$ which is thought to control Cr(VI) concentrations in some soils (Rai et al., 1988).

Baron et al. (1996) identified $KFe_3(CrO_4)_2(OH)_6$ in a Cr(VI)-contaminated soil. The relatively low solubility of $KFe_3(CrO_4)_2(OH)_6$ suggests that this solid can form in large parts of a Cr(VI)-contaminated aquifer, affecting Cr(VI)-mobility and interfering with clean-up efforts (Baron and Palmer, 1996b). $KFe_3(CrO_4)_2(OH)_6$ is the structural analog of jarosite ($KFe_3(SO_4)_2(OH)_6$), a sulfate mineral that commonly occurs in sulfate-rich acidic environments such as acid sulfate soils (Van Breemen, 1973) and acid mine drainage (Chapman et al., 1983; Alpers et al., 1989).

Jarosite and its chromate analog are members of the jarosite-alunite group of isostructural minerals and solids with the general formula $AB_3(XO_4)_2(OH)_6$. The jarosite crystal structure can accommodate a wide variety of ions and extensive substitution and formation of solid solutions have been reported in natural minerals and in synthetic solids. The A site is occupied most commonly by K^+(jarosite), Na^+ (natrojarosite), and H_3O^+ (hydronium jarosite). Solid solution formation between these endmembers is common and most natural jarosites exhibit at least some substitution (Parker, 1962; Kubisz, 1964; Brophy and Sheridan, 1965; Alpers et al., 1989). The B position is most commonly occupied by Fe^{3+} (jarosite) and Al^{3+} (alunite) but other ions such as Cr^{3+} (Townsend et al., 1986), Ga^{3+}, and In^{3+} (Dutrizac and Kaiman, 1976) have also been reported in synthetic solids. A solid solution between jarosite and alunite has been documented for both natural and synthetic solids (Brophy et al., 1962). The oxyanion position (XO_4^{2-}) in jarosites and alunites is most commonly occupied by SO_4^{2-} but partial substitution by PO_4^{2-}, AsO_4^{3-}, CO_3^{2-}, SbO_4^{3-}, CrO_4^{2-}, SiO_4^{4-} in natural minerals (Scott, 1987) and complete substitution by SeO_4^{2-} in synthetic solids (Dutrizac et al., 1981) have also been reported. Recently, Savage et al. (2000) also documented partial substitution by AsO_4^{3-} in natural jarosites.

* Author to whom correspondence should be addressed (dbaron@csub.edu).

Table 1. Summary of Synthesis and Composition of $KFe_3(Cr_XS_{1-X})O_4)_2(OH)_6$ Solid Solutions.

	Solution 1		Solution 2				
	H_2O (mL)	$Fe(NO_3)_3 \cdot 9H_2O$ (g)	H_2O (mL)	K_2CrO_4 (g)	K_2SO_4 (g)	Solid Composition	Munsell Color
JAR-05	45	30.29	45	9.22	0.44	$K_{0.92}Fe_{2.80}(Cr_{0.90}S_{0.10}O_4)_2(OH)_6$	2.5YR 4/8
JAR-10	45	30.29	45	8.73	0.87	$K_{0.94}Fe_{2.80}(Cr_{0.80}S_{0.20}O_4)_2(OH)_6)$	5YR 5/8
JAR-25	45	30.29	45	7.28	2.18	$K_{0.96}Fe_{3.12}(Cr_{0.53}S_{0.47}O_4)_2(OH)_6$	5YR 5/8
JAR-30	45	30.29	45	6.80	2.61	$K_{1.00}Fe_{3.14}(Cr_{0.42}S_{0.58}O_4)_2(OH)_6$	7.5YR 5/8
JAR-40	45	20.19	45	5.82	3.48	$K_{0.92}Fe_{2.84}(Cr_{0.27}S_{0.73}O_4)_2(OH)_6$	7.5YR 5/8
JAR-50	45	10.10	45	4.85	4.35	$K_{1.00}Fe_{2.86}(Cr_{0.17}S_{0.83}O_4)_2(OH)_6$	7.5YR 6/8
JAR-80	45	20.19	45	1.94	6.96	$K_{0.98}Fe_{2.98}(Cr_{0.09}S_{0.91}O_4)_2(OH)_6$	2.5Y 6/8

Sulfate and chromate ions have an equivalent charge, similar structure, and similar thermochemical radii, 2.30 Å for sulfate and 2.40 Å for chromate (Waddington, 1959). The thermochemical radius of a non-spherical ion is the equivalent ionic radius for that ion calculated from the lattice energy of compounds containing these non-spherical ions (Huheey, 1972). The similarity of the chromate and sulfate ions and the fact that jarosite and $KFe_3(CrO_4)_2(OH)_6$ have the same crystal structure, and the extensive documented solid solution formation in the jarosite/alunite group suggest that solid solutions ($KFe_3(Cr_XS_{(1-X)}O_4)_2(OH)_6$) between $KFe_3(CrO_4)_2(OH)_6$ and jarosite exist. Sulfate is a common groundwater constituent and is also present in chrome-plating solutions, one of the primary sources of chromium contamination, and it is likely that such solid solutions could form at many chromium-contaminated sites. The aqueous Cr(VI) concentrations in solutions equilibrated with such solid solution phases would be dramatically different from concentrations in solutions equilibrated with pure $KFe_3(CrO_4)_2(OH)_6$. The presence of these solid solution phases would thus have important implications for the mobility of Cr(VI) and the remediation of contaminated sites.

Despite the common solid solution formation in natural and synthetic jarosites, and despite the strong effect on solubility caused by partial substitution of different ions in the alkali and oxyanion positions, little work has been done to examine the solubility and thermodynamic properties of such solid solutions. To our knowledge, a study by Alpers et al. (1989) on the solubility of K-H_3O-Na jarosites precipitated from acid mine drainage waters, and a study by Stoffregen and Cygan (1990) on Na-K exchange between alunite and aqueous sulfate solutions are the only exceptions.

The purpose of this paper is to investigate solid solutions between jarosite and its chromate analog and to measure the thermodynamic parameters required to evaluate the potential impact of such solid solutions on the mobility of chromium in contaminated soils. The specific objectives are: (1) to determine if a complete solid solution series exists between jarosite and its chromate analog; (2) to characterize these solid solution phases; (3) to measure the solubility of solid solution phases with a range of Cr/S ratios under the acidic conditions in which these solids are expected to form; and (4) to determine an appropriate model to describe the solid solution/aqueous solution reactions of these phases.

2. EXPERIMENTAL METHODS

2.1. Synthesis of KFe_3 $(CR_x5_{(1-X)}O_4)_2(OH)_6$ Solid Solutions

$KFe_3(Cr_XS_{(1-X)}O_4)_2(OH)_6$ solid solutions were synthesized by controlled mixing of a solution of $Fe(NO_3)_3 \cdot 9H_2O$ and a solution of K_2CrO_4 and K_2SO_4 at 95°C. For the ferric nitrate solution, 10.10 to 30.29 g of $Fe(NO_3)_3 \cdot 9H_2O$ were added to 45 mL of water, and for the potassium chromate/sulfate solutions, 1.94 to 9.22 g of K_2CrO_4 and 0.44 to 6.96 g of K_2SO_4 were added to 45 mL of water. Reagent grade chemicals and ultrapure water (18 megaohm cm) were used for the synthesis and all experiments. The amounts of K_2CrO_4 and K_2SO_4 were varied in individual syntheses to obtain synthetic solids with different Cr/S ratios. The compositions of the synthesis solutions are summarized in Table 1. The two solutions were slowly (50 mL h^{-1}) added to a covered beaker containing an initial 10 mL of ultrapure water. The resulting solution was kept at 95°C and stirred at a moderate rate (100 rpm) using a stirrbar. After 3 h, the precipitates were allowed to settle and the residual solution decanted. The precipitates were then washed thoroughly and dried at 110°C for 24 h. The syntheses of jarosite and $KFe_3(CrO_4)_2(OH)_6$ are described in Baron and Palmer (1996a, 1996b).

2.2. Characterization of KFe_3 $(Cr_xS_{(1-x)}O_4)_2(OH)_6$ Solid Solutions

Small amounts of the precipitates were digested in HCl and analyzed for K and Fe using a Perkin Elmer Model 603 atomic absorption spectrometer (AAS), Cr(VI) using the diphenylcarbazide (DPC) method (APHA, 1985) and a Perkin Elmer Lambda 20 UV-visible spectrometer, and SO_4 using high performance ion chromatography (HPIC). All synthetic solids were characterized by powder X-ray diffraction (XRD) with a Rigaku Bi-Plane diffractometer using Cu Kα radiation (1.54056 Å). Solids were examined with a Zeiss 960 Digital scanning electron microscope (SEM) with a Link energy dispersive X-ray spectrometer (EDX). The synthetic solids were also analyzed by thermogravimetric analysis (TGA) with a Perkin Elmer Pyris 7 TGA to determine the amount of water in the crystal structure and confirm the overall stoichiometry. Approximately 5 to 10 mg of the synthetic solids were heated from 100°C to 900°C at 10°C/min while the mass was continuously recorded.

2.3. Dissolution Experiments

Dissolution experiments with the synthetic $KFe_3(Cr_XS_{(1-X)}O_4)_2(OH)_6$ solid solutions were conducted at 23.0±1.0°C. For the dissolution experiments, 200 mg of synthetic solid were added to 200 mL of ultrapure water with the pH adjusted to 2.0 using $HClO_4$. The solutions were placed in polyethylene bottles that were placed on a shaker running at approximately 50 rpm. The experiments were sampled over time to monitor the evolution of the solution during the dissolution process and to determine when a steady state was achieved. For each experiment, 10 samples were taken. The first nine samples were taken within the first five months after the experiment was initiated; a final sample was taken almost three years after the start of the experiment. For each sample, 4 mL of the $KFe_3(Cr_XS_{(1-X)}O_4)_2(OH)_6$ suspension was

Table 2. Powder X-ray Diffraction Analysis of $KFe_3(Cr_XS_{(1-X)}O_4)_2(OH)_6$ Solid Solutions.

			d-spacing (A)						
h	k	l	Jar 05	Jar 10	Jar 25	Jar 30	Jar 40	Jar 50	Jar 80
1	0	1	6.02	6.00	6.00	5.96	5.96	5.94	5.95
0	0	3	5.82	5.79	5.77	5.75	5.75	5.73	5.69
0	1	2	5.17	5.15	5.14	5.11	5.12	5.09	5.09
1	1	0	3.71	3.70	3.68	3.68	3.67	3.66	3.66
1	0	4	3.60	3.59	3.57	3.57	3.57	3.57	3.55
0	2	1	3.16	3.15	3.14	3.13	3.12	3.12	3.11
1	1	3	3.12	3.11	3.10	3.09	3.09	3.09	3.08
2	0	2	3.02	3.01	3.00	2.99	2.98	2.97	2.97
0	0	6	2.91	2.90	2.89	2.88	2.87	2.86	2.85
0	2	4	2.58	2.58	2.57	2.56	2.56	2.55	2.54
1	2	2	2.322	2.316	2.305	2.299	2.293	2.291	2.308
0	3	3	2.007	2.002	1.994	1.990	1.988	1.984	1.980
0	2	7	1.965	1.961	1.953	1.947	1.945	1.941	1.934
0	0	9	1.936	1.932	1.924	1.916	1.916	1.911	1.901
2	2	0	1.852	1.849	1.840	1.836	1.836	1.833	1.829
2	0	8	1.801	1.804	1.788	1.786	1.783	1.779	1.771
2	2	3	—	1.759	1.752	1.749	1.746	1.745	1.740
3	1	2	1.740	1.739	1.732	1.731	1.728	1.725	1.720
1	1	9	1.717	1.713	1.705	1.700	—	1.694	—
1	3	4	1.646	1.645	1.637	1.635	—	1.629	1.626
1	2	8	1.621	1.618	1.612	1.605	1.603	1.600	1.595
4	0	1	1.598	1.594	1.588	1.584	1.583	1.580	1.578
3	1	5	1.584	1.581	1.574	1.573	1.569	1.572	1.565
0	4	2	1.575	1.573	1.569	1.565	1.563	1.556	1.558
2	2	6	1.561	1.558	1.551	1.549	1.546	1.554	1.544
Unit Cell Dimensions									
a-axis (Å)			7.408	7.389	7.361	7.349	7.337	7.331	7.319
			±0.002	±0.002	±0.003	±0.003	±0.003	±0.006	±0.002
c-axis (Å)			17.448	17.406	17.312	17.523	17.132	17.209	17.109
			±0.010	±0.011	±0.011	±0.012	±0.015	±0.024	±0.011
Volume ($Å^3$)			829.3 ± 1.0	823.0 ± 1.1	812.2 ± 1.1	806.9 ± 1.1	803.4 ± 1.4	800.8 ± 2.4	793.8 ± 1.0

withdrawn. The samples were filtered using a 0.1μm polysulfonate filter to remove suspended solids and then analyzed for pH, K and Fe using AAS, Cr(VI) using the DPC method, and SO_4^{2-} using HPIC. The last sample was analyzed for K, Fe, and Cr using a Perkin Elmer Elan 6100 Inductively Coupled Plasma Mass Spectrometer, and for sulfate using a Dionex DX-120 Ion Chromatograph. Since the experiments were conducted in oxidizing $HClO_4$ solutions and no reductants capable of reducing ferric iron were present, it was assumed that all Fe was present as ferric iron. The uncertainty associated with the analytical measurements is ±10%. The precision of the standard pH buffer solutions used in calibrations for the pH measurements is ±0.02 pH units. The solids remaining in the dissolution experiments after 1090 d were examined by XRD and SEM/EDX to determine whether secondary solids had formed in the experiments.

3. RESULTS

3.1. Solid Characterization

The synthesis yielded between 3.5 and 5 g of precipitates. In general, the solutions with higher concentrations of ferric nitrate yielded a larger amount of solid. The precipitates vary in color between the yellow of jarosite and red of $KFe_3(CrO_4)_2(OH)_6$ (Table 1). Wet chemical analysis of the precipitates indicates the stoichiometry of the synthetic solids is close to that of jarosite-type compounds (Table 1). The molar ratios of Cr/S in the solid vary from 0.90/0.10 to 0.09/0.91. The solids are impoverished in Cr compared to the synthesis solutions. For example, solid JAR-50 synthesized from a solution with equimolar concentrations of Cr and S, has a Cr/S molar ratio of 0.17/0.83. Most of the synthetic solids have a slight K and Fe deficit compared to the 'ideal' formula. Such deficits are commonly observed in natural and synthetic jarosites (e.g., Brophy and Sheridan, 1965; Kubisz, 1970; Härtig et al., 1984; Baron and Palmer, 1996a) and in synthetic $KFe_3(CrO_4)_2(OH)_6$ (Baron and Palmer, 1996b). The K deficit is generally attributed to substitution of H_3O^+ (hydronium) for K^+. The charge imbalance caused by the Fe deficit is generally thought to be balanced by substitution of H_2O for some of the OH^- groups in the crystal structure (Härtig et al., 1984; Baron and Palmer, 1996a).

The synthetic solids were identified as jarosite-type compounds by comparing powder X-ray diffraction patterns with those reported for jarosite and $KFe_3(CrO_4)_2(OH)_6$ in PDF cards 22–827 and 20–894 (JCPDS, 1994). The XRD peaks produced by the synthetic compounds are listed in Table 2. All the peaks produced by the precipitates are consistent with jarosite-type compounds. The absence of unidentified peaks indicates that no other crystalline phases are present in the precipitates at detectable levels. The X-ray peaks of the solid-solution phases are not broadened compared to the pure end-member phases. Peak broadening would be expected if the composition of the solids varied locally.

The unit cell volume of $KFe_3(CrO_4)_2(OH)_6$ is larger than that of jarosite and the corresponding XRD peaks are shifted toward slightly smaller angles, representing the slightly larger

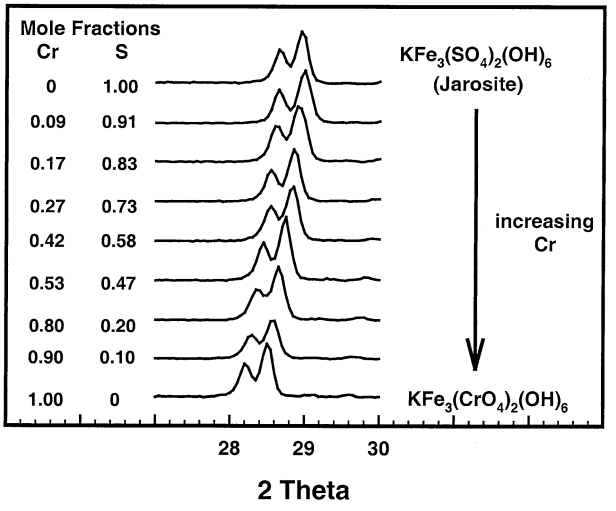

Fig. 1. Main powder X-ray diffraction peaks of $KFe_3(Cr_XS_{(1-X)}O_4)_2(OH)_6$ solid solutions.

d-spacings of $KFe_3(CrO_4)_2(OH)_6$. As the Cr content of the synthetic solids increases, the peaks generally shift toward lower angles and correspondingly larger *d*-spacings (Table 2).

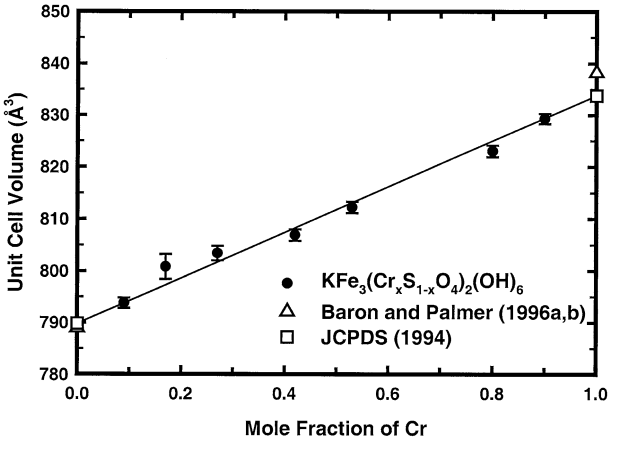

Fig. 2. Unit cell volume of $KFe_3(Cr_XS_{(1-X)}O_4)_2(OH)_6$ solid solutions as a function of composition. The solid line is a linear interpolation between the unit cell volumes for the endmembers reported in PDF files 22–827 and 20–894.

Figure 1 shows the region around the two strongest jarosite peaks (27−30° 2θ) as an example of this shift. Such a continuous shift indicates a solid-solution series rather than a mixture of two phases. In a mixture, distinct sets of peaks from each phase would be present. The intensity of these peaks would vary as a function of the fraction of each separate phase in the mixture.

The unit cell volume of the $KFe_3(Cr_XS_{(1-X)}O_4)_2(OH)_6$ solid solutions is reasonably represented by a linear function of composition between the sulfate and chromate endmembers (Fig. 2, Table 2), also indicating a continuous solid solution. A linear relation between composition and unit cell size has often been taken as an indicator for an ideal solid solution (e.g., Königsberger et al., 1991). However, it is important to note that small departures from linearity can indicate a rather large departure from ideality. For example, the $(Ba,Sr)SO_4$ series was initially considered ideal partly because of apparently linear variation of cell size. Several researchers have more recently claimed non-ideality for the series (Glynn, 2000; Hanor, 2000).

Examination of samples of solids Jar-50 and Jar-25 with SEM/EDX showed that the precipitates consist of multicrystalline particles ranging in size from 5 to 50 μm and having uniform concentrations of K, Fe, Cr, and S. No other phases with a different composition were observed.

Thermogravimetric analysis was conducted by heating the synthetic solids from 100 to 900°C at a rate of 10°C/min. The total mass loss over this interval ranges from 21.5 to 38.5 mass percent with the mass loss increasing with the mole fraction of chromate in the solids (Table 3). The thermogravimetric analysis of the synthetic solid Jar 25 (Fig. 3) is used as an example of the thermal degradation of the solid solutions. The upper curve is the mass loss versus temperature and the lower curve its derivative. Four peaks in the derivative curve show that the mass loss occurs in four principal temperature intervals: (1) a small initial mass loss between 100 and 280°C, represented by a peak in the derivative curve at ~220°C, (2) a major mass loss between 280 and 430°C, represented by a peak at 380°C and a shoulder in this peak at 340°C, (3) another smaller mass loss between 430 and 600°C, represented by a broad peak at approximately 480°C, and (4) and a final major mass loss between 600 and 800°C, represented by a peak at 720°C.

The general pattern of the thermal degradation can be explained by a combination of the thermal degradation of jarosite (Brophy and Sheridan, 1965; Baron and Palmer, 1996a) and its

Table 3. Summary of the Thermogravimetric Analysis of $KFe_3(Cr_XS_{(1-X)}O_4)_2(OH)_6$ Solid Solutions.

Temperature Range (°C)	Weight Loss (%)													
	Jar 05		Jar 10		Jar 25		Jar 30		Jar 40		Jar 50		Jar 80	
	M[1]	T[2]	M	T	M	T	M	T	M	T	M	T	M	T
100–280	1.5	2.3	2.0	2.2	3.0	2.1	2.5	1.6	3.0	2.0	2.5	2.3	2.5	2.8
280–430	12.0	10.1	10.5	10.2	11.0	10.4	12.0	10.5	12.0	10.6	12.0	10.7	12.0	10.7
430–60	6.0	6.0	5.5	5.4	3.5	3.6	3.0	2.8	2.0	1.8	2.0	1.1	1.0	0.6
600–800	2.0	2.4	4.5	4.8	11.0	11.3	13.0	13.9	16.0	17.5	18.0	19.9	23.0	21.8
Total	21.5	20.8	22.5	22.5	28.5	27.3	30.5	28.8	33.0	31.9	34.5	34.0	38.5	36.0

[1] M = Measured value.
[2] T = Theoretical value.

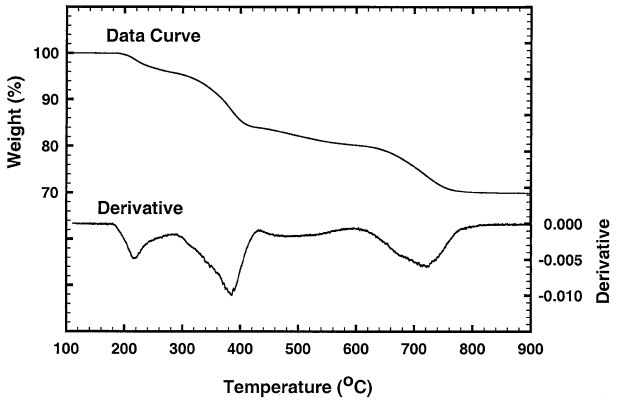

Fig. 3. Thermogravimetric analysis of synthetic solid Jar-25 as an example of the thermal breakdown of $KFe_3(Cr_XS_{(1-X)}O_4)_2(OH)_6$ solid solutions.

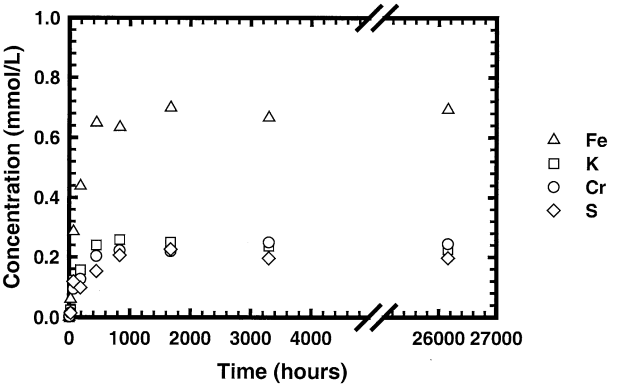

Fig. 4. Dissolution of synthetic solid Jar-25 as an example of the dissolution of $KFe_3(Cr_XS_{(1-X)}O_4)_2(OH)_6$ solid solutions.

chromate analog (Baron and Palmer, 1996b). The mass loss in the first interval between 100 and 280°C is due to the loss of H_2O from hydronium substituting for potassium and the loss of H_2O substituting for OH^- to balance the charge imbalance caused by the Fe deficit in the solids (Baron and Palmer, 1996a; Härtig et al., 1984; Kubisz, 1970). The second mass loss in the interval between 280°C and 430°C corresponds to a combination of (1) the breakdown of the $KFe_3(SO_4)_2(OH)_6$ component into $KFe(SO_4)_2$ and Fe_2O_3 and the associated release of 3 mol of water per mole of jarosite; and (2) and the breakdown of the $KFe_3(CrO_4)_2(OH)_6$ component into $K_2CrO_4{\bullet}Fe_2(CrO_4)_3$, and Fe_2O_3 and the loss of 3 mol of water per mole of $KFe_3(CrO_4)_2(OH)_6$. The third mass loss in the interval between 430°C and 600°C corresponds to the breakdown of $K_2CrO_4{\bullet}Fe_2(CrO_4)_3$ into K_2CrO_4 and Fe_2O_3, and CrO_3. The CrO_3 produced by this breakdown is subsequently reduced and transformed to the Cr(III) compound Cr_2O_3 (Cotton and Wilkinson, 1988). This overall reaction results in the release of 9/8 mol of O_2 per mole of $KFe_3(CrO_4)_2(OH)_6$. The fourth and final mass loss in the interval between and 600°C and 800°C corresponds to the breakdown of $KFe(SO_4)_2$ into K_2SO_4 and Fe_2O_3 and the release of 1.5 mol of SO_3 per mole of jarosite.

Thermogravimetric analyses for all the synthetic solids are summarized in Table 3. Generally, the mass losses observed in the different temperature intervals correspond closely to the theoretical losses expected based on the chemical analysis of the solids, thus further confirming the overall composition and the chromate to sulfate ratio of the solids.

3.2. Dissolution Experiments

In the dissolution experiments, the bulk of the reaction occurred within the first week of the experiment with dissolution rates declining with time (Fig. 4). Dissolution of the solids is generally stoichiometric, with the mole fractions of total Cr(VI) and total SO_4^{2-} in the aqueous solutions close to the mole fraction of Cr and S in the solids. The only exception is solid JAR-30 with a solid Cr/S ratio of 0.42/0.58. The average of the aqueous Cr/S ratios from all the samples of JAR-30 taken after stoichiometric saturation was attained is 0.47/0.53. However, even in this case, the discrepancy is within the analytical error of ±10% associated with the chromium and sulfate measurements. Within the time frame of the experiments, there is no noticeable enrichment of either Cr or S in the solutions as the dissolution process proceeds or after a steady state has been established.

A steady state was attained in the dissolution experiments after ~40 d. The compositions of the solutions after 1090 d are summarized in Table 4. For all samples, aqueous activities of K^+, Fe^{3+}, CrO_4^{2-}, and SO_4^{2-} were calculated using the geochemical speciation model MINTEQA2 (Allison et al., 1990). Activity corrections were made using the Davies equation as incorporated into MINTEQA2. The MINTEQA2 thermodynamic database was modified to include the $FeHSO_4^{2+}$ and $FeCrO_4^+$ complexes. Other species included in the calculations and thermodynamic data used are listed in Table 5. The aqueous mole fractions of Cr(VI) ($Cr(VI)_{total}/(Cr(VI)_{total}+S(VI)_{total})$) and S(VI) ($S(VI)_{total}/(Cr(VI)_{total}+S(VI)_{total})$), and the aqueous activities calculated from the last four samples taken at 39, 68, 138, and 1090 d after a steady state was attained, are listed in Table 6.

Table 4. Final Aqueous Concentrations in the Dissolution Experiments.

	Sample Time (days)	pH	$[K]_{tot}$ mol L^{-1}	$[Fe(III)]_{tot}$ mol L^{-1}	$[Cr(VI)]_{tot}$ mol L^{-1}	$[S(VI)]_{tot}$ mol L^{-1}
Jar-05	1090	2.07	$2.42*10^{-4}$	$6.71*10^{-4}$	$4.50*10^{-4}$	$4.02*10^{-5}$
Jar-10	1090	2.07	$2.28*10^{-4}$	$7.75*10^{-4}$	$3.93*10^{-4}$	$9.81*10^{-5}$
Jar-25	1090	2.05	$2.26*10^{-4}$	$6.93*10^{-4}$	$2.44*10^{-4}$	$1.97*10^{-4}$
Jar-30	1090	2.04	$2.38*10^{-4}$	$6.84*10^{-4}$	$2.15*10^{-4}$	$2.30*10^{-4}$
Jar-40	1090	2.05	$2.32*10^{-4}$	$6.06*10^{-4}$	$1.65*10^{-4}$	$3.60*10^{-4}$
Jar-50	1090	2.05	$1.59*10^{-4}$	$5.51*10^{-4}$	$8.50*10^{-5}$	$3.70*10^{-4}$
Jar-80	1090	2.05	$2.30*10^{-4}$	$4.85*10^{-4}$	$3.60*10^{-5}$	$4.10*10^{-4}$

Table 5. Thermodynamic Data Used for Speciation Calculations.

Reaction	log K_{298}	Ref.
Aqueous Species		
$Fe^{3+} + SO_4^{2-} \leftrightarrow FeSO_4^+$	3.92	1
$Fe^{3+} + SO_4^{2-} + H^+ \leftrightarrow FeHSO_4^{2+}$	2.48	2
$Fe^{3+} + 2SO_4^{2-} \leftrightarrow Fe(SO_4)_2^-$	5.42	1
$Fe^{3+} + CrO_4^{2-} \leftrightarrow FeCrO_4^+$	7.8	3
$Fe^{3+} + OH^- \leftrightarrow FeOH^{2+}$	−2.19	1
$Fe^{3+} + 2OH- \leftrightarrow Fe(OH)_2^+$	−5.67	4
$2Fe^{3+} + 2OH- \leftrightarrow Fe_2(OH)_2^{4+}$	−2.95	1
$K^+ + SO_4^{2-} \leftrightarrow KSO_4^-$	0.85	1
$K^+ + CrO_4^{2-} \leftrightarrow KCrO_4^-$	0.799	1
$H^+ + CrO_4^{2-} \leftrightarrow HCrO_4^-$	6.55	7
$2CrO_4^{2-} + 2H^+ - H_2O \leftrightarrow Cr_2O_7^{2-}$	14.7	7
$2H^+ + CrO_4^{2-} \leftrightarrow H_2CrO_4^0$	6.31	6
$H^+ + SO_4^{2-} \leftrightarrow HSO_4^-$	1.98	5
$OH^- + H^+ \leftrightarrow H_2O_{(l)}$	13.998	1
Solid Phases		
$KFe_3(CrO_4)_2(OH)_{6(s)} \leftrightarrow K^+ + 2CrO_4^{2-} + 3Fe^{3+} + 6H_2O - 6H^+$	−18.4 ± 0.6	8
$KFe_3(SO_4)_2(OH)_{6(s)} \leftrightarrow K^+ + 2SO_4^{2-} + 3Fe^{3+} + 6H_2O - 6H^+$	−11.0 ± 0.3	9

References: (1) Allison et al. (1990); (2) Ball et al. (1987); (3) Baron and Palmer (1996b); (4) Nordstrom and Munoz (1994); (5) Cox et al. (1989); (6) Ball and Nordstrom (1998); (7) Palmer et al. (1987); (8) Baron and Palmer (1998); (9) Baron and Palmer (1996a).

The XRD scans of the region around the two major jarosite peaks (27 to 30° 2θ) of the solids remaining in the dissolution experiments after 1090 d are shown in Figure 5b. There is no indication of the formation of secondary jarosite phases with compositions different from the original solids. The complete scans (Fig. 5a) do not show any evidence for the formation of other secondary solids in the dissolution experiment.

4. DISCUSSION

Seven $KFe_3(Cr_XS_{(1-X)}O_4)_2(OH)_6$ solid solutions with a wide range of Cr/S ratios were synthesized and characterized. Syntheses from solutions with higher $Fe(NO_3)_3 \cdot 9H_2O$ concentrations generally yielded a larger amount of solid, indicating that Fe was the limiting element in these solutions. All synthetic solids are enriched in S compared to the Cr/S ratios of the

Table 6. Calculated Ion Activities from the Dissolution Experiments for the Last Four Samples.

	Time (days)	pH	log $\{K^+\}$	log $\{Fe^{3+}\}$	log $\{SO_4^{2-}\}$	log $\{CrO_4^{2-}\}$	Aqueous Cr Mole Fraction	calculated log IAP_{SS}
Jar-05 (X=0.90)	39	3.06	−3.62	−3.81	−4.86	−8.01	0.91	−18.08 ± .25
	68	2.09	−3.63	−3.83	−5.01	−7.99	0.93	−17.96 ± .25
	138	2.07	−3.67	−3.89	−4.96	−7.97	0.92	−18.26 ± .25
	1090	2.07	−3.66	−3.86	−4.97	−7.99	0.92	−18.20 ± .25
Jar-10 (X=0.80)	39	2.07	−3.66	−3.83	−4.56	−8.09	0.78	−17.46 ± .25
	68	2.09	−3.66	−3.80	−4.58	−8.05	0.80	−17.20 ± .25
	138	2.06	−3.69	−3.87	−4.57	−8.05	0.80	−17.61 ± .25
	1090	2.07	−3.69	−3.80	−4.60	−8.06	0.80	−17.41 ± .25
Jar-25 (X=0.53)	39	2.06	−3.63	−3.87	−4.14	−8.25	0.52	−15.48 ± .25
	68	2.06	−3.65	−3.84	−4.23	−8.31	0.49	−15.55 ± .25
	138	2.05	−3.67	−3.85	−4.29	−8.25	0.56	−15.66 ± .25
	1090	2.05	−3.69	−3.84	−4.29	−8.27	0.55	−15.71 ± .25
Jar-30 (X=0.42)	39	2.05	−3.67	−3.88	−4.29	−8.36	0.50	−15.01 ± .25
	68	2.08	−3.66	−3.80	−4.22	−8.35	0.46	−14.49 ± .25
	138	2.05	−3.69	−3.88	−4.22	−8.30	0.50	−14.90 ± .25
	1090	2.04	−3.67	−3.84	−4.23	−8.33	0.48	−14.85 ± .25
Jar-40 (X=0.27)	39	2.04	−3.65	−3.87	−4.03	−8.56	0.27	−13.48 ± .25
	68	2.08	−3.56	−3.87	−4.03	−8.45	0.30	−13.09 ± .25
	138	2.05	−3.69	−3.92	−4.01	−8.49	0.32	−13.54 ± .25
	1090	2.05	−3.68	−3.92	−4.00	−8.42	0.31	−13.53 ± .25
Jar-50 (X=0.17)	39	2.05	−3.64	−3.79	−4.10	−8.83	0.20	−12.42 ± .25
	68	2.07	−3.60	−3.87	−4.02	−8.76	0.18	−12.35 ± .25
	138	2.05	−3.63	−3.89	−4.01	−8.75	0.18	−12.54 ± .25
	1090	2.05	−3.85	−3.95	−3.98	−8.70	0.19	−12.96 ± .25
Jar-80 (X=0.09)	39	2.03	−3.58	−3.78	−3.99	−9.08	0.09	−11.64 ± .25
	68	2.07	−3.66	−3.87	−3.97	−9.10	0.08	−11.71 ± .25
	138	2.05	−3.71	−3.92	−3.98	−9.03	0.10	−12.04 ± .25
	1090	2.05	−3.68	−4.01	−3.92	−9.05	0.08	−12.17 ± .25

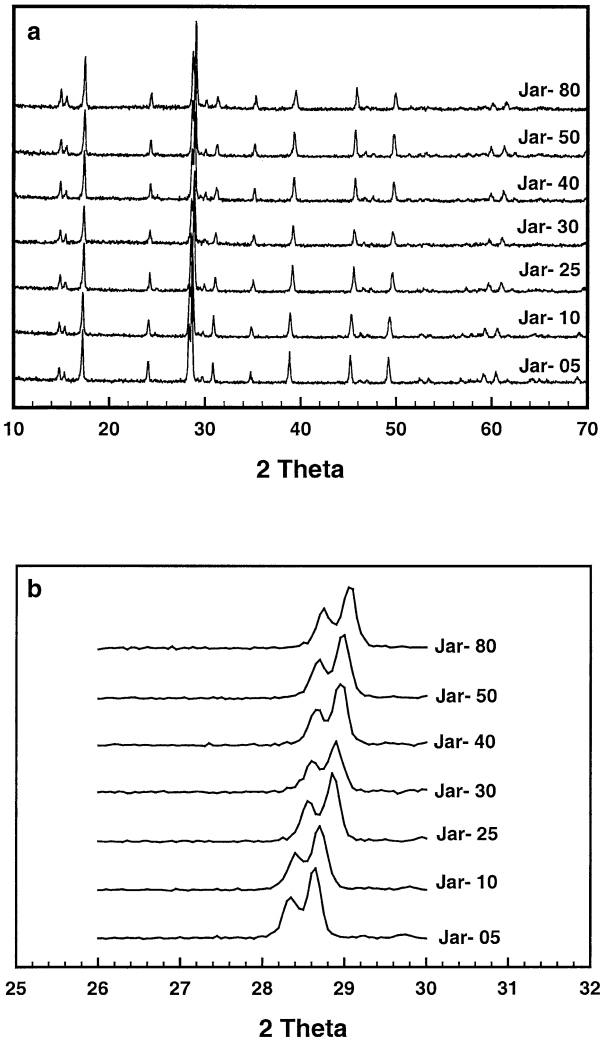

Fig. 5. Powder X-ray diffraction of the solids remaining in the dissolution experiments after 1090 d: (a) complete scans, and (b) close-up of the region around the two main peaks.

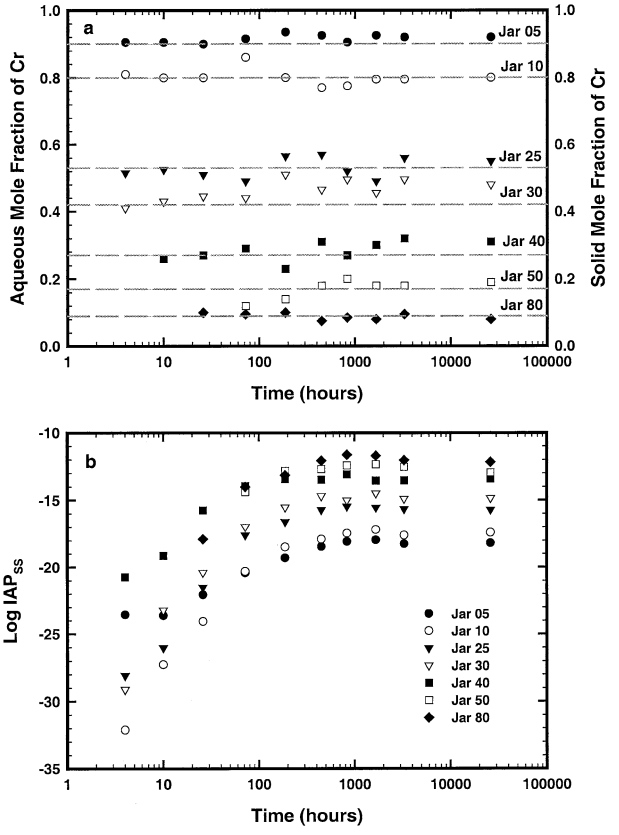

Fig. 6. Dissolution of solid solution phases: (a) mole fraction of aqueous Cr over time, and (b) log IAP_{SS} values over time. In (a), the data points are the aqueous mole fractions of Cr from samples and the dashed lines represent the solid mole fractions of Cr in the solids.

synthesis solutions. This is surprising because the solubility product of $KFe_3(CrO_4)_2(OH)_6$ is 7 orders of magnitude lower than that of jarosite. One possible explanation for the preferential incorporation of sulfate is that in the acidic synthesis solutions, Cr(VI) is present primarily as $HCrO_4^-$ and the concentration of CrO_4^{2-}, which is incorporated into the solid is low compared to the concentration of total Cr(VI). Sulfur, however, is present primarily as SO_4^{2-}. Another explanation could be that the kinetics of ion incorporation under the conditions of very high supersaturation in the solid syntheses favor sulfate over chromate. Fernández-González et al. (1999) also observed preferential partitioning of SO_4^{2-} over CrO_4^{2-} during the precipitation of $Ba(Cr,S)O_4$ solid solutions.

The dissolution process of the solid solutions is stoichiometric, with the mole fractions of total Cr(VI) and total SO_4^{2-} in the solutions close to the mole fractions of Cr and S in the solids (Fig. 6a). After approximately 40 d, the solutions reach a steady state and a stoichiometric saturation state is attained. Stoichiometric dissolution and the attainment of a stoichiometric saturation state are often observed during the dissolution of solid solutions (Thorstenson and Plummer, 1977). The stoichiometric saturation state for the dissolution of a solid solution was first defined by Thorstenson and Plummer (1977) for "situations where the composition of the solid phase remains invariant, owing to kinetic restrictions, even though the solid is part of a continuous compositional series." Under such circumstances, solids behave as a one-component solid phase with unit activity. Glynn (1990) further points out that the stoichiometric saturation concept may apply to situations where the reaction time is sufficiently short, the solid to aqueous solution ratio is sufficiently high, and the solid is relatively insoluble. In our case, the slow dissolution and precipitation kinetics and the relatively low solubility of these solids may contribute to the fact that these solids do not move towards thermodynamic equilibrium in the time frame of this study.

For the stoichiometric dissolution of $KFe_3(Cr_XS_{(1-X)}O_4)_2(OH)_6$ solid solutions according to

$$KFe_3(Cr_XS_{(1-X)}O_4)_2(OH)_6 + 6H^+ \leftrightarrow K^+ + 3Fe^{3+} + 2X\,CrO_4^{2-} + (2-2X)\,SO_4^{2-} + 6H_2O \quad (1)$$

a stoichiometric ion activity product, IAP_{SS} can be written as

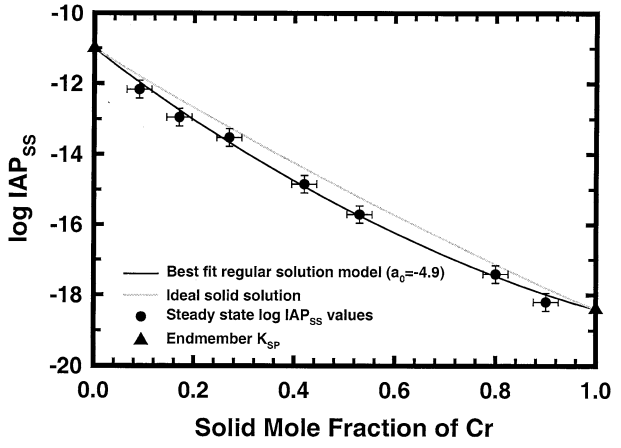

Fig. 7. Final Log IAP_{SS} values, representing log K_{SS} values, as a function of the mole fraction of Cr in the solids. The solid black line represents a hypothetical ideal solid solution. The solid gray line represents the best-fit regular solution model ($a_0 = -4.9$). The K_{SP} values for the endmembers are from Baron and Palmer (1996a, 1996b).

$$IAP_{SS} = \{K^+\}\{Fe^{3+}\}^3\{CrO_4^{2-}\}^{2X}\{SO_4^{2-}\}^{(2-2X)}\{H_2O\}^6\{H^+\}^{-6} \quad (2)$$

where brackets denote activity. The log IAP_{ss} is then given by

$$\log IAP_{SS} = \log\{K^+\} + 3\log\{Fe^{3+}\} + 2X\log\{CrO_4^{2-}\} + (2-2X)\log\{SO_4^{2-}\} + 6\log\{H_2O\} + 6\,pH \quad (3)$$

When a state of stoichiometric saturation is attained, IAP_{SS} equals the stoichiometric saturation constant, K_{SS}. The log IAP_{SS} values were calculated using Eqn. 3 with the assumption that $\{H_2O\}=1$. Fig. 6b shows a plot of log IAP_{SS} values for the all samples versus time. After approximately 40 d, a steady state is achieved and the ion activity products from the last 4 samples do not show any variation beyond the analytical uncertainty. In general, the ion activity products calculated from the third and fourth to last samples are slighty higher than those from the last two samples. However, the differences are within the analytical uncertainty of ± 0.25 log units. For the subsequent calculations, we assumed that the last sample taken after 1090 d is representative for the stoichiometric saturation state. Slightly different results would be obtained if one used one of the other steady state samples or an average.

Log IAP_{SS} values from the sample taken after 1090 d (Table 6) are shown as a function of the solid mole fraction of Cr in Figure 7. The analytical error associated with the log IAP_{SS} values calculated from the precision of the analytical measurements ($\pm 10\%$) and the precision of the pH buffer solutions (± 0.02 pH units) is 0.25 log units (assuming that the covariance between these parameters equals zero). The error associated with the aqueous concentrations of Cr and S is the analytical error of 10%. In addition to this analytical error, there is error associated with the uncertainties in the associated thermodynamic data used in calculating the ion activities and hence the IAP_{ss}. The errors reported in Table 6 refer only to the analytical error.

As previously discussed, the synthetic solids have a composition slightly different from the ideal composition on which Eqn. 3 is based. However, using Eqn. 3 with the ideal stoichiometry is consistent with previous work on the solubility of jarosite and its chromate analog and appears justified since the non-ideality is only slight. If one was to use the actual composition as determined by chemical analysis, calculated ion activity products would be up to 0.5 log units lower than those calculated using the ideal stoichiometry.

The last samples taken after 1090 d are the best representation of the stoichiometric saturation state, thus, we have used the log IAP_{SS} values calculated from these samples to represent the log K_{SS} values. A plot of these log K_{SS} values versus solid mole fraction of Cr (Fig. 7), shows that the log K_{SS} values are close to, but consistently lower than what would be expected for an ideal solid solution, suggesting a negative excess free energy of mixing.

Assuming that a stoichiometric saturation state was attained in the dissolution experiments, the excess free energy of mixing, G^E, for a binary solid solution can be calculated from

$$G^E = RT\,[\ln K_{SS} - X(\ln K_{CA} + \ln X) - (1-X)(\ln K_{BA} + \ln(1-X))], \quad (4)$$

where K_{CA} and K_{BA} are the solubility products of CA and BA, respectively (Glynn and Reardon, 1990). The Guggenheim (1937, 1952) expansion series for G^E

$$G^E = X(1-X)RT\,[a_0 + a_1(X-(1-X)) + a_2(X-(1-X))^2\ldots], \quad (5)$$

where a_0, a_1, etc. are dimensionless coefficients, is commonly used to represent the excess free energy of a binary solid solution as a function of composition. Combining Eqns. 4 and 5 and writing them for $KFe_3(Cr_XS_{(1-X)}O_4)_2(OH)_6$ while using only the first coefficient, a_0, (regular solution model) yields

$$\ln K_{SS} = X(1-X)a_0 + (1-X)\ln[K_{Jar}(1-X)] + X\ln[K_{CrJar}X)], \quad (6)$$

where K_{Jar} and K_{CrJar} are the solubility products of the two endmember solids. Fitting our K_{SS} values as a function of solid composition to Eqn. 6 yields a best fit with $a_0 = -4.9 \pm 0.8$ ($n = 7$, $df = 6$, $r^2 = 0.994$, $t = 6.17$) where the uncertainty term is the standard error of the fitted parameter. The data were also fit using a two-parameter Guggenheim model, however, the a_1 parameter (0.6 ± 2.1) is not significantly different from zero at the 5% significance level ($t = 0.280$; $df = 5$) indicating that the model is over-parameterized. Thus, the data are better represented by a single parameter Guggenheim expansion (regular solution model). The possibility exists that the deviation from ideality is an artifact of the non-stoichiometry of the solids, namely the small K and Fe deficits. The non-stoichiometry can affect the solubility of the solids and thus the calculated K_{SS} values and the a_0 value based on them. Unfortunately, in the absence of information on how the non-stoichiometry affects solubility this effect cannot be quantified. However, the deviations from stoichiometry are random, therefore, we do not believe that they are the reason for the systematic deviation from ideality observed in the calculated K_{SS} values.

The negative value for a_0 suggests that the excess free energy of mixing is negative and that mixing is energetically

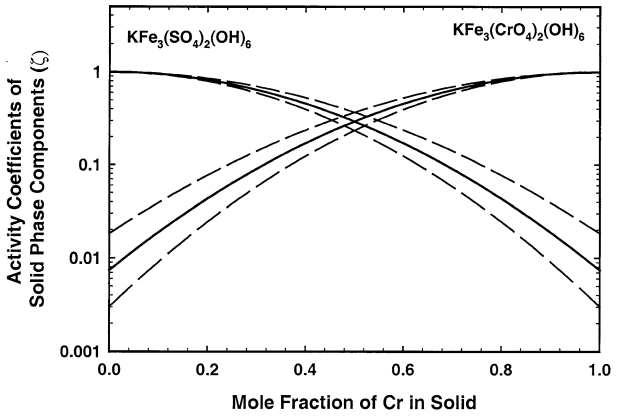

Fig. 8. Activity coefficients of the endmember solid phase components in the solid solutions as a function of composition. Dashed lines represent the uncertainty associated with the estimate of a_0.

favored, implying a certain degree of ordering in the solid solutions. Based on the calculated a_0, the Margules parameter, W, is -12 ± 2 kJ/mol. The activity coefficients of $KFe_3(CrO_4)_2(OH)_6$ (ζ_{CrJar}) and $KFe_3(SO_4)_2(OH)_6$ (ζ_{Jar}) as components of the solid solution can then be calculated as a function of composition using the relationships

$$\ln \zeta_{CrJar} = (1 - X)^2 a_0 \quad (7)$$

$$\ln \zeta_{Jar} = a_0 X^2 \quad (8)$$

where X is the mole fraction of Cr in the solid (Redlich and Kister, 1948). The solid phase activity coefficients vary with composition of the solid phase and range from unity when the mole fraction of the solid phase component is equal to one to 0.0074 as the mole fraction approaches zero (Fig. 8).

Calculations using MINTEQA2 (Allison et al., 1990) illustrate the effect that the presence of these solid solution phases would have on groundwater at a contaminated site in a simple scenario. Using the regular solution model with $a_0 = -4.9$ and assuming that the solids dissolve stoichiometrically at pH 4 and no secondary precipitates form, dissolution of $KFe_3(Cr_{0.25}S_{0.75}O4)_2(OH)_6$ to a stoichiometric saturation state would result in a total aqueous Cr(VI) concentration of 4.3×10^{-6} M. The total Cr(VI) concentration calculated using an ideal solid solution model (a_0=0, stoichiometric saturation state) is 5.1×10^{-6} M. In contrast, the Cr(VI) concentration from dissolution of pure $KFe_3(CrO_4)_2(OH)_6$ under the same conditions is 2.8×10^{-5} M. Clearly, these differences are of concern when evaluating the possible presence of Cr(VI)-containing solids at contaminated sites and cleaning up these sites. For example, pump-and-treat remediation for the scenario outlined above would require pumping 6.5 times the number of pore volumes if the same mass of Cr(VI) is present as a solid solution rather than pure $KFe_3(CrO_4)_2(OH)_6$.

To gain further insight into the $KFe_3(Cr_XS_{(1-X)}O_4)_2(OH)_6$ solid solution, we used the excess free energy data calculated from the stoichiometric saturation model to construct a Lippmann diagram. A Lippmann diagram is based on the total solubility product, $\Sigma\Pi$, which for the $KFe_3((Cr_X,S_{1-X})O_4)_2(OH)_6$ solid solution can be written as

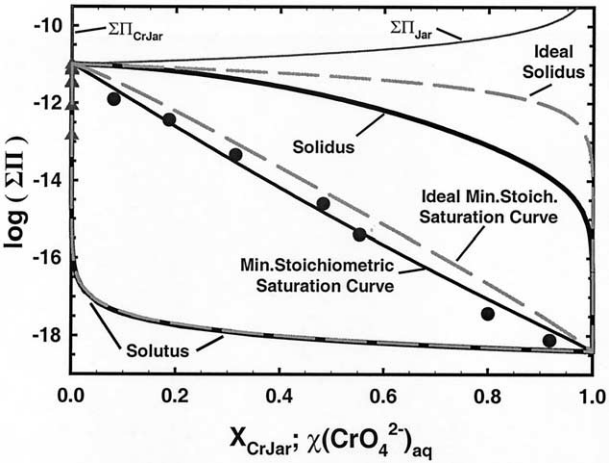

Fig. 9. Lippmann diagram for $a_0 = -4.9$ (solid lines) and the ideal case when $a_0 = 0.0$ (dashed lines). The X_{CrJar} scale is associated with the solidus curve, while the $\chi(CrO_4^{2-})_{aq}$ scale is associated with the solutus curve. The $\Sigma\Pi_{CrJar}$ curve, the solutus, and the solutus for the ideal case are all superimposed on one another over most of the diagram. The triangles denote the data using aqueous activity fractions and the circles are based on the total aqueous concentrations.

$$\Sigma\Pi = \{K^+\}\{Fe^{3+}\}^3\{H_2O\}^6\{H^+\}^{-6}[\{SO_4^{2-}\} + \{CrO_4^{2-}\}]^2 \quad (9)$$

A Lippmann diagram is typically constructed (Glynn and Reardon, 1990) by first plotting

$$\Sigma\Pi = a_{Jar} \cdot K_{Jar} + a_{CrJar} \cdot K_{CrJar} = X_{Jar} \cdot \zeta_{Jar} \cdot K_{Jar} + X_{CrJar} \cdot \zeta_{CrJar} \cdot K_{CrJar} \quad (10)$$

against X_{CrJar} (solidus curve) where a_{CrJar} and a_{Jar}, and X_{CrJar} and X_{Jar} denote the activities and mole fractions of the $KFe_3(CrO_4)_2(OH)_6$ and $KFe_3(SO_4)_2(OH)_6$ solid phase components, respectively. All the other parameters have been previously defined. Then

$$\Sigma\Pi = \left(\frac{\chi(SO_4^{2-})_{aq}}{K_{Jar}\zeta_{jar}} + \frac{\chi(CrO_4^{2-})_{aq}}{K_{CrJar}\zeta_{CrJar}}\right)^{-1} \quad (11)$$

is plotted against $\chi(CrO_4^{2-})_{aq}$ (solutus curve) on the same scale as X_{CrJar}, where

$$\chi(CrO_4^{2-})_{aq} = \frac{\{CrO_4^{2-}\}^2}{\{SO_4^{2-}\}^2 + \{CrO_4^{2-}\}^2} \quad (12)$$

and

$$\chi(SO_4^{2-})_{aq} = \frac{\{SO_4^{2-}\}^2}{\{SO_4^{2-}\}^2 + \{CrO_4^{2-}\}^2} \quad (13)$$

are the "aqueous activity fractions" of CrO_4^{2-} and SO_4^{2-}, respectively (see Addendum).

A Lippmann diagram for the $KFe_3(Cr_XS_{(1-X)}O_4)_2(OH)_6$ solid solution for $a_0 = -4.9$ (solid lines) and the ideal case when $a_0 = 0.0$ (dashed lines) is shown in Figure 9. In addition to the solutus and the solidus, we have plotted the saturation curves for pure $KFe_3(CrO_4)_2(OH)_6$ ($\Sigma\Pi_{CrJar}$) and pure $KFe_3(SO_4)_2(OH)_6$ ($\Sigma\Pi_{Jar}$). These curves are calculated by

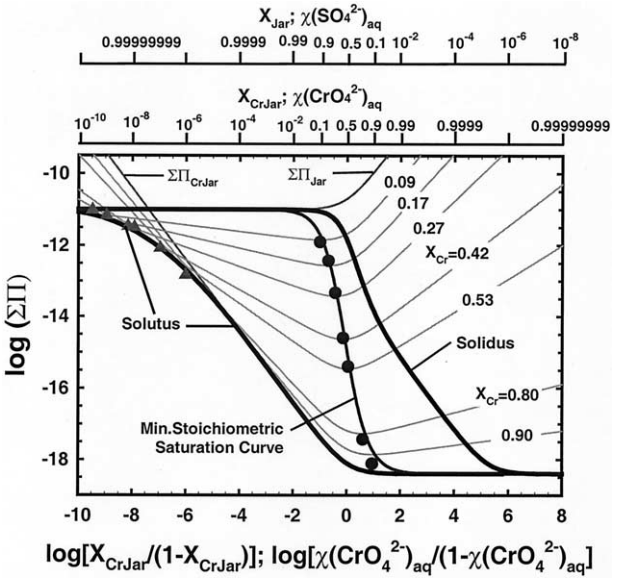

Fig. 10. Modified Lippmann diagram for the $KFe_3(Cr_XS_{(1-X)}O_4)_2(OH)_6$ solid solution with stoichiometric saturation curves, the minimum stoichiometric saturation curve, and the experimental data superimposed. Triangles are for experimentally determined IAP_{ss} data plotted against $\chi(CrO_4^{2-})_{aq}$. Circles indicate calculated IAP_{ss} based on the mole fractions of the total Cr(VI) and S(VI) concentrations. The X_{CrJar} and $1-X_{CrJar}$ scales are associated with the solidus curve whilst the $\chi(CrO_4^{2-})$ and $1-\chi(CrO_4^{2-})$ scales are associated with the solutus curve.

$$\Sigma\Pi_{CrJar} = \frac{K_{CrJar}}{\chi(CrO_4^{2-})_{aq}} \tag{14}$$

and

$$\Sigma\Pi_{Jar} = \frac{K_{Jar}}{\chi(SO_4^{2-})_{aq}} \tag{15}$$

respectively. In Fig. 9, the $\Sigma\Pi_{CrJar}$ curves plot very close to the solutus curve over the entire range of $\chi(CrO_4^{2-})_{aq}$.

A key difficulty with the traditional Lippmann diagram in Figure 9 is that the aqueous activity fractions of chromate are 4 to 5 orders of magnitude smaller than the mole fractions of chromate in the solid and the aqueous mole fractions based on total chromium and total sulfate in solution. The mole fraction scale could be plotted on a semilogarithmic scale; however, the diagram becomes difficult to read at relatively low mole fractions of SO_4^{2-}. A modified Lippmann diagram was therefore constructed (Fig. 10) where log ($\Sigma\Pi$) was plotted against $\log[X_{CrJar}/(1-X_{CrJar})]$ and against $\log[\chi(CrO_4^{2-})_{aq}/(1-\chi(CrO_4^{2-})_{aq})]$. This scaling on the abscissa allows us to view the diagram at very low values of X_{CrJar}, $(1-X_{CrJar})$, $\chi(CrO_4^{2-})_{aq}$, and $(1-\chi(CrO_4^{2-})_{aq})$. One can now see that for $\chi(CrO_4^{2-})_{aq} < 10^{-5}$, the saturation state of the solid solution becomes distinguishable from that of the pure phase. For convenience, we have included two additional axes above the diagram for the mole and activity fractions of CrO_4^{2-} and SO_4^{2-}.

As $KFe_3(Cr_XS_{(1-X)}O_4)_2(OH)_6$ dissolves in acidic solutions, the Cr(VI) is converted primarily into $HCrO_4^-$ and $Cr_2O_7^{2-}$ aqueous species and only a small fraction remains as CrO_4^{2-}. The modified Lippmann diagram illustrates that if the rate of dissolution of the original $KFe_3(Cr_XS_{(1-X)}O_4)_2(OH)_6$ solid solution is slower than the rate of precipitation of secondary phases, the solid precipitated at primary saturation will be a fairly pure $KFe_3(CrO_4)_2(OH)_6$ with $X_{CrJar} > 0.99$ when $\chi(CrO_4^{2-})_{aq} > 3 \times 10^{-4}$. To reach thermodynamic equilibrium within the range of X_{CrJar} used in this study, the $\chi(CrO_4^{2-})_{aq}$ would have to be $< 3 \times 10^{-5}$ due to the large difference in the solubility product of the endmembers. It should be emphasized that these small values of the activity fractions are a consequence of the Cr(VI) speciation and the fractions of total Cr(VI) would be orders of magnitude greater.

The key problem with using the total solubility product to illustrate solid-solution/aqueous-solution reactions for $KFe_3(Cr_xS_{(1-x)}O_4)_2(OH)_6$ is that our observations clearly indicate that dissolution is stoichiometric. The Lippmann diagram is useful nonetheless if we superimpose stoichiometric saturation curves for each of the solids used in the present study on the modified Lippman diagram (Fig. 10). These stoichiometric saturation curves were calculated using

$$\Sigma\Pi_{SS} = \frac{K_{SS}}{[1-\chi(CrO_4^{2-})_{aq}]^{1-X}[\chi(CrO_4^{2-})_{aq}]^{X}} \tag{16}$$

where X is the mole fraction of chromate in the solids. In addition, the minimum stoichiometric saturation curve, i.e., the curve connecting the minimum values of each of the stoichiometric saturation curves, is plotted in Figures 9 and 10. The triangles are the $\Sigma\Pi_{ss}$ values plotted against $\chi(CrO_4^{2-})_{aq}$. Although it is impossible to tell from Fig. 9, it can readily be seen in the modified Lippmann diagram (Fig. 10) that these data plot along the solutus curve. However, they are not at the appropriate thermodynamic equilibrium points. The data could indicate that the solutions were at primary saturation points suggesting the formation of a secondary phase. However, the data plot in an area where the stoichiometric saturation curves converge toward the solutus and the data do plot close to their corresponding stoichiometric saturation curves. In general, the location of data points on a Lippmann diagram will depend on the aqueous speciation, degree to which secondary phases are formed, and the relative rates of dissolution and precipitation. If there was no speciation, then the concentration of CrO_4^{2-} would be equal to $Cr(VI)_{total}$ and SO_4^{2-} would be equal to $S(VI)_{total}$. The minimum in a stoichiometric saturation curve occurs where $\chi(CrO_4^{2-})_{aq} = X_{CrJar}$, (Glynn and Reardon, 1990). If no secondary phases have precipitated and the stoichiometric saturation model is appropriate, $\Sigma\Pi_{ss}$ values calculated from $\chi(CrO_4^{2-})_{aq} = X_{CrJar}$, should plot along the minimum stoichiometric saturation curve. We calculated $\Sigma\Pi_{ss}$ values using Eqn. 16 and the previously calculated K_{ss} values, but assumed that $\chi(CrO_4^{2-})_{aq} = (Cr(VI)_{total}/(Cr(VI)_{total}+S(VI)_{total}))$ and $\chi(SO_4^{2-})_{aq} = (S(VI)_{total}/(Cr(VI)_{total}+S(VI)_{total}))$. The data, shown by the circles in Fig. 10, do plot along the minimum stoichiometric saturation curve and they are close to their respective stoichiometric saturation curves indicating that the aqueous mole fractions based on the total concentrations of Cr(VI) and S(VI) are equal to X_{CrJar} and X_{Jar}, respectively. We therefore conclude that over the time scale of our experiments the stoichiometric saturation model

adequately describes the dissolution of $KFe_3(Cr_XS_{(1-X)}O_4)_2(OH)_6$ solid solutions and the data represented by the triangles in Fig. 10, do not plot at the minimum of the stoichiometric saturation curves only due to aqueous speciation.

An interesting application of Figure 10 is the possibility of determining the composition of the solid phase that is in contact with a solution that is at stoichiometric saturation with respect to the solid. If there is sufficient information to calculate ionic activities, then $\log[\chi(CrO_4^{2-})_{aq}/(1-\chi(CrO_4^{2-})_{aq}]$ can be determined and the IAP_{ss} calculated using Eqn. 2. The value of X_{CrJar} can be calculated from Eqn. 6 using an appropriate numerical technique such as Newton iteration. Convergence should be attained in < 5 iterations even when the initial guess is far from the actual value. The feasibility of making such calculations is suggested in Fig. 10. In the region to the right of the $\Sigma\Pi(CrO_4)$ curve, the stoichiometric saturation curves are subparallel and the values of X_{CrJar} are unique for a given $\chi(CrO_4^{2-})_{aq}$ and $\Sigma\Pi_{ss}$. However, in the region to the left of the $\Sigma\Pi_{CrJar}$ curve, the stoichiometric saturation curves cross each other and the values of $\Sigma\Pi_{ss}$ are not unique. Therefore, a simple test for the feasibility of determining the solid phase composition from the aqueous phase composition is if the $\Sigma\Pi$ calculated from Eqn. 9 is greater than $\Sigma\Pi_{CrJar}$ calculated from Eqn. 14.

5. SUMMARY AND CONCLUSIONS

Seven $KFe_3(Cr_XS_{(1-X)}O_4)_2(OH)_6$ solids with a wide range of Cr/S ratios were synthesized. The reaction pathways were observed during the dissolution of these solid solutions. Several key observations of these experiments are: 1) sulfate is preferentially incorporated into solids from the acidic synthesis solutions; 2) the unit cell volume of the solid solution varies as a near-linear function of composition; 3) the solid solution dissolves stoichiometrically and reaches a steady state (stoichiometric saturation state) after approximately 40 d; and 4) the stoichiometric saturation state is maintained for at least three years.

Calculated log K_{SS} values suggest that the solid solution is close to ideal with a small negative excess free energy of mixing. The excess free energy of mixing can be modeled with a regular solution model with $a_0 = -4.9 \pm 0.8$.

A modified Lippmann diagram was constructed based on the calculated excess free energy data. For $\chi(CrO_4^{2-})_{aq} > 10^{-5}$, the saturation curve for pure $KFe_3(CrO_4)_2(OH)_6$ plots close to the solutus curve. Under these conditions, the saturation state of the solution for the solid solution is indistinguishable from that of the pure phase. Plotting the $\Sigma\Pi_{ss}$ values on the Lippmann diagram suggests that under some conditions, it is not possible to uniquely determine the composition of the dissolving solid phase from the composition of the resulting solution at stoichiometric saturation with respect to the solid solution.

The observation that sulfate is incorporated preferentially into $KFe_3(Cr_XS_{(1-X)}O_4)_2(OH)_6$ from acidic synthesis solutions implies that the formation of such solids is possible even in environments with only moderate sulfate concentrations. $KFe_3(Cr_XS_{(1-X)}O_4)_2(OH)_6$ maintains lower aqueous concentrations of Cr(VI) than pure $KFe_3(CrO_4)_2(OH)_6$ and therefore could limit Cr(VI) mobility even more than pure $KFe_3(CrO_4)_2(OH)_6$.

More work is to required to elucidate the precipitation pathways in the $KFe_3(CrO_4)_2(OH)_6$ - $KFe_3(SO_4)_2(OH)_6$ - H_2O system. In addition, we need to determine the times scales for the solid solution-aqueous solution system to evolve from stoichiometric saturation to thermodynamic equilibrium

6. ADDENDUM

6.1. Derivation of Equations for Construction of Lippman Diagram for the Solid Solution $A(B_{1-X}C_X)_\alpha$

For a solid solution with the composition $A(B_{1-X}CX)_\alpha$, the reaction of the individual components, AB_α and AC_α are written as

$$AB_\alpha \Leftrightarrow A + \alpha B \tag{A1}$$

$$AC_\alpha \Leftrightarrow A + \alpha C \tag{A2}$$

and the equilibrium expressions are

$$\{A\}\{B\}^\alpha = K_{AB_\alpha} X_{AB_\alpha} \zeta_{AB_\alpha} \tag{A3}$$

$$\{A\}\{C\}^\alpha = K_{AC_\alpha} X_{AC_\alpha} \zeta_{AC_\alpha} \tag{A4}$$

where X_{AB_α} and X_{AC_α} and ζ_{AB_α} and ζ_{AC_α} are the mole fractions and activity coefficients of the AB_α and AC_α components in the solid solution. Adding Eqs. (A3) and (A4) yields

$$\{A\}(\{B\}^\alpha + \{C\}^\alpha) = K_{AB_\alpha} X_{AB_\alpha} \zeta_{AB_\alpha} + K_{AC_\alpha} X_{AC_\alpha} \zeta_{AC_\alpha} = \Sigma\Pi \tag{A5}$$

where $\Sigma\Pi$ denotes the "total solubility product." For the problem of a binary solid solution with an arbitrary stoichiometric coefficient, α, we define the activity fractions as

$$\chi(B)_{aq} = \frac{\{B\}^\alpha}{\{B\}^\alpha + \{C\}^\alpha} \tag{A6}$$

$$\chi(C)_{aq} = \frac{\{C\}^\alpha}{\{B\}^\alpha + \{C\}^\alpha} \tag{A7}$$

Solving Eqs. (A6) and (A7) for $\{B\}^\alpha$ and $\{C\}^\alpha$, respectively, and then substituting the results into Eqs. (A3) and (A4) yields

$$\frac{\{A\}(\{B\}^\alpha + \{C\}^\alpha)\chi(B)_{aq}}{K_{AB_\alpha}\zeta_{AB_\alpha}} = X_{AB_\alpha} \tag{A8}$$

$$\frac{\{A\}(\{B\}^\alpha + \{C\}^\alpha)\chi(C)_{aq}}{K_{AC_\alpha}\zeta_{AC_\alpha}} = X_{AC_\alpha} \tag{A9}$$

Adding Eqn. (A8) and (A9) we get

$$\{A\}(\{B\}^\alpha = \{C\}^\alpha)\left[\frac{\chi(B)_{aq}}{K_{AB_\alpha}} + \frac{\chi(C)_{aq}}{K_{AC_\alpha}}\right] = X_{AB_\alpha} + X_{AC_\alpha} = 1 \tag{A10}$$

Substituting eqn. (A5) into (A10) and solving for $\Sigma\Pi$, we obtain

$$\Sigma\Pi = \frac{1}{\frac{\chi(B)_{aq}}{K_{AB_\alpha}\zeta_{AB_\alpha}} + \frac{\chi(C)_{aq}}{K_{AC_\alpha}\zeta_{AC_\alpha}}} \quad (A11)$$

which is the equation of the solutus as given by Glynn and Reardon (1990).

The stoichiometric ion activity product, IAP_{SS}, is given by

$$IAP_{SS} = \{A\}\{B\}^{\alpha(1-X)}\{C\}^{\alpha X} \quad (A12)$$

Multiplying Eq. (A12) by $(\{B\}^{\alpha}+\{C\}^{\alpha})/(\{B\}^{\alpha}+\{C\}^{\alpha})$ and rearranging the terms yields

$$IAP_{SS} = \{A\}(\{B\}^{\alpha} + \{C\}^{\alpha}) \frac{\{B\}^{\alpha X_{AB_\alpha}}}{(\{B\}^{\alpha} + \{C\}^{\alpha})^{X_{AB_\alpha}}} \frac{\{C\}^{\alpha X_{AC_\alpha}}}{(\{B\}^{\alpha} + \{C\}^{\alpha})^{X_{AC_\alpha}}} \quad (A13)$$

or

$$\Sigma\Pi_{SS} = \frac{IAP_{SS}}{\chi(B)_{aq}^{X_{AB_\alpha}}\chi(C)_{aq}^{X_{AC_\alpha}}} \quad (A14)$$

which identical to the equation for the solid solution curves given by Glynn and Reardon (1990). Subsituting Eqn. (A12) into Eqn. (A14) and taking the limit as X_{AB_α} approaches unity yields the end-member equation:

$$\Sigma\Pi_{AB_\alpha} = \frac{\{A\}\{B\}^{\alpha}}{\chi(B)_{aq}} = \frac{K_{AB_\alpha}}{\chi(B)_{aq}} \quad (A15)$$

Similarly, taking the limit as X_{AC_α} approaches unity, yields the other end-member equation:

$$\Sigma\Pi_{AC_\alpha} = \frac{\{A\}\{C\}^{\alpha}}{\chi(C)_{aq}} = \frac{K_{AC_\alpha}}{\chi(C)_{aq}} \quad (A16)$$

Thus, the equations needed to construct a Lippmann diagram for a binary solid solution with composition $A(B_{1-X}CX)_\alpha$, are the same as the equations for a solid solution for which α is equal to unity, if the activity fractions are defined by equations (A6) and (A7).

Acknowledgments—The manuscript has greatly benefited from insightful comments by Pierre Glynn, Carlos M. Pina, and two anonymous reviewers. The authors thank Sara Draucker for her assistance with the XRD analyses. This work was supported under a grant from the U.S. Environmental Protection Agency, Office of Exploratory Research. This paper has not been reviewed by the U.S. EPA and does not necessarily reflect the views of the agency. Additional funding was provided by the CSUB Research Council.

Associate editor: J. Schott

REFERENCES

Allison J. D., Brown D. S., Novo-Gradac K. J. (1990) *MINTEQA2/PRODEFA2*, a geochemical assessment model for environmental systems: version 3.0. U. S. Environmental Protection Agency, Athens, GA.

Alpers C. N., Nordstrom D. K., and Ball J. W. (1989) Solubility of jarosite solid solutions precipitated from acid mine waters, Iron Mountain, California, U.S.A.. *Sci. Géol. Bull.* **42,** 281–298.

Amonette J. E. and Rai D. (1990) Identification of noncrystalline $(Fe,Cr)(OH)_3$ by infrared spectroscopy. *Clays Clay Min.* **42,** 281–298.

APHA (1985) *Standard methods for the examination of water and wastewater*. American Public Health Association, Washington, DC.

Ball J. W., Nordstrom D. K., Zachmann D. W. (1987) WATEQ4F. A personal computer FORTRAN translation of the geochemical model WATEQ2 with revised data base. *U.S.G.S. Open-File Report.* 87–150.

Ball J. W. and Nordstrom D. K. (1998) Critical evaluation and selection of standard state thermodynamic properties for chromium metal and its aqueous ions, hydrolysis species, oxides and hydroxides. *J. Chem. Eng. Data.* **43,** 895–918.

Baron D. and Palmer C. D. (1996a) Solubility of jarosite at 4–35°C. *Geochim. Cosmochim. Acta* **60,** 185–195.

Baron D. and Palmer C. D. (1996b) Solubility of $KFe_3(CrO_4)_2(OH)_6$ at 4–35°C. *Geochim. Cosmochim. Acta* **60,** 3815–3824.

Baron D. and Palmer C. D. (1998) Solubility of $KFe(CrO_4)_2$-$2H_2O$ at 4–75°C. *Appl. Geochem.* **12,** (8) 961–973.

Baron D., Stanley J. T., and Palmer C. D. (1996) Identification of two iron-chromate precipitates in a Cr(VI)-contaminated soil. *Env. Sci. Tech.* **30,** 964–968.

Brophy G. P., Scott E. S., and Snellgrove R. A. (1962) Sulfate studies II. Solid solution between alunite and jarosite. *Am. Mineral.* **47,** 112–126.

Brophy G. P. and Sheridan M. F. (1965) Sulfate studies. IV. The jarosite-natrojarosite-hydronium jarosite solid solution series. *Am. Mineral.* **50,** 1595–1607.

Calder L. M. (1988) Chromium contamination of groundwater. In *Chromium in the Natural and Human Environments* (eds. J. O. Nriagu and E. Nieboer), pp. 215–579. John Wiley and Sons, New York.

Chapman B. M., Jones D. R., and Jung R. F. (1983) Processes controlling metal ion attenuation in acid mine drainage streams. *Geochim. Cosmochim. Acta.* **47,** 1957–1973.

Cotton F. A. and Wilkinson G. (1998) Wiley.

Cox J. D., Wagman D. D., and Mededev V. A. (1989) *CODATA Key Values for Thermodynamics*. Hemisphere Publishing Corporation.

Dutrizac J. E., Dinardo O., and Kaiman S. (1981) Selenate analogs of jarosite-type compounds. *Hydrometall.* **6,** 327–337.

Dutrizac J. E. and Kaiman S. (1976) Synthesis and properties of jarosite-type compounds. *Can. Mineral.* **6,** 327–337.

Fernández-González A., Diaz R. M., and Prieto M. (1999) Crystallisation of $Ba(SO_4,CrO_4)$ solid solutions from aqueous solutions. *J. Cryst. Growth* **200,** 227–235.

Glynn P. (1990) Modeling solid-solution reactions in low temperature systems. In *Chemical Modeling of Aqueous Systems II*, Vol. 416 (eds. D. C. Melchior and R. L. Bassett), pp. 74–87. American Chemical Society Symposium Series.

Glynn P. D. and Reardon E. J. (1990) Solid-solution aqueous solution equilibria: thermodynamic theory and representation. *Am. J. Sci.* **290,** 164–201.

Glynn P. (2000). Solid-solution solubilities and thermodynamics: sulfates, carbonates, and halides. In *Sulfate minerals—crystallography, geochemistry, and environmental significance.* (eds. C. N. Alpers, J. L. Jambor and D. K. Nordstrom), Reviews in Mineralogy and Geochemistry,**40**, Mineralogical Society of America, Washington, D.C.

Guggenheim E. A. (1937) Theoretical basis of Raoult's law. *Trans. Faraday Sec.* **33,** 151–159.

Guggenheim E. A. (1953) *Mixtures*. Oxford University Press, London.

Hanor J. S. (2000). Barite-celestine geochemistry and environments of formation. In *Sulfate minerals—crystallography, geochemistry, and environmental significance.* (eds. C. N. Alpers, J. L. Jambor and D. K. Nordstrom), Reviews in Mineralogy and Geochemistry,**40,** Mineralogical Society of America, Washington, D.C.

Härtig C., Brand P., and Bohmhammel K (1985) Fe-Al-Isomorphie und Strukturwasser in Kristallen vom Jarosit-Alunit Typ. Z. *Anorg. Allg. Chem.* **508,** 159–164.

Huheey J. E. (1972) *Inorganic Chemistry*. Harper & Row, New York.

JCPDS (Joint Committee on Powder Diffraction Standards) (1994) Powder diffraction file. Swarthmore, Pennsylvania, International Center for Diffraction Data.

Königsberger E., Hausner R., and Gamsjäger H. (1991) Solid-solute phase equilibria in aqueous solution V. The system Cd^{2+}-Ca^{2+}-CO_2-H_2O. *Geochim. Cosmochim. Acta.* **55,** 3505–3514.

Kubisz J. (1964) A study of minerals in the alunite-jarosite group. *Polska Akad. Nauk, Prace Geol.* **22,** 1–93.

Kubisz J. (1970) Studies on synthetic alkali-hydronium jarosite. I. Synthesis of jarosite and natrojarosite. *Mineral. Pol.* **3,** 23–27.

Van Breemen N. (1973) Soil forming processes in acid sulfate soils. In *Acid Sulfate Soils, Proc. Int. Symp. on Acid Sulfate Soils* (ed. H. Dost), Vol I Publ. 18 ILRI, 66–130. Wageningen, The Netherlands.

Nordstrom D. K. and Munoz J. L. (1994) *Geochemical Thermodynamics*. 2nd Edition. Blackwell Scientific Publications, Boston, Mass.

Palmer C. D. and Wittbrodt P. R. (1991) Processes affecting the Remediation of chromium-contaminated sites. *Env. Health. Perspect.* **92,** 25–40.

Palmer D. A., Wesolowski D., and Mesmer R. E. A. (1987) Potentiometric investigation of the hydrolysis of chromate(VI) ion in NaCl media to 175°C. *J. Sol. Chem.* **92,** 25–40.

Parker R. L. (1962) Isomorphous substitution in natural and synthetic alunite. *Am. Min.* **47,** 127–136.

Rai D., Sass B. M., and Moore D. A. (1987) Chromium(III) hydrolysis constants and solubility of chromium(III) hydroxides. *Inorg. Chem.* **26,** 345–349.

Rai D., Zachara J. M., Eary L. E., Ainsworth C. C., Amonette J. E., Cowan C. E., Szelmeczka R. W., Resch C. T., Schmidt R. L., Smith S. C., Girvin D. C. (1988) Chromium reactions in geologic materials. Electric Power Research Institute Report EA-5741, Palo Alto, CA.

Redlich O., Kister A. T. (1948) Algebraic representation of thermodynamic properties and the classification of solutions. *Ind. Eng. Chem.* **40**, 345–348.

Rytuba J. J., Kleinkopf M. D. (1995) Silica-carbonate mercury deposits. In *Preliminary compilation of descriptive geoenvironmental mineral deposit models* (ed. E. A. DuBray), USGS Open File Report 95–831, 199– 203.

Sass D. M. and Rai D. (1987) Solubility of amorphous chromium(III)-iron(III) hydroxide solid solutions. *Inorg. Chem.* **26,** 228–2232.

Savage K. S., Tingle T. N., O'Day P. A., Waychunas G. A., and Bird D. K. (2000) Arsenic speciation in pyrite and secondary weathering phases, Mother Lode Gold District, Tuolumne County, California. *Appl. Geochem.* **15,** 1219–1244.

Scott M. S. (1987) Solid solution in, and classification of, gossan-derived members of the alunite-jarosite family, northwest Queensland, Australia. *Am. Mineral.* **72,** 178–187.

Stoffregen R. E. and Cygan G. L. (1990) An experimental study of Na-K exchange between alunite and aqueous sulfate solutions. *Am. Mineral.* **75,** 209–220.

Thorstenson D. C. and Plummer L. N. (1977) Equilibrium criteria for two component solids reacting with fixed composition in an aqueous-phase; example: the magnesian calcites. *Am. J. Sci.* **277,** 1203–1223.

Townsend M. G., Longworth G., and Roudaut E. (1986) Triangular-spin, kagome plane in jarosites. *Phys. Rev. B.* **33,** 4919–4926.

Pub. 18 ILRIVan Breemen N. (1973) Soil forming processes in acid sulfate soils. *Acid Sulfate Soils, Proc. Int. Symp. on Acid Sulfate Soils*, Vol I (ed. H. Dost), pp. 66–130. Wageningen, The Netherlands.

Waddington T. C. (1959) Lattice energies. In *Advances in inorganic chemistry and radiochemistry*, Vol. 1 (eds. H. J. Emeléus and A. G. Sharpe), pp. 157–221. Academic Press, Inc., New York.